

Article

On the Adaptation of an AUV into a Dedicated Platform for Close Range Imaging Survey Missions

Yevgeni Gutnik * , Aviad Avni, Tali Treibitz and Morel Groper

The Hatter Department of Marine Technologies, Leon H. Charney School of Marine Sciences, University of Haifa, 199 Aba Khoushy Ave. Mount Carmel, Haifa 3498838, Israel; aavni@univ.haifa.ac.il (A.A.); ttreibitz@univ.haifa.ac.il (T.T.); mgroper@univ.haifa.ac.il (M.G.)

* Correspondence: ygutnik@campus.haifa.ac.il; Tel.: +972-548022772

Featured Application: Underwater autonomous high-resolution imaging seabed surveys, precise motion control of autonomous underwater vehicles

Abstract: This study presents the redesign of an existing autonomous underwater vehicle (AUV) with limited maneuverability, transforming it into a platform optimized for autonomous, near-seabed visual imaging missions. This work describes the enhancement of the AUV's maneuverability through the addition of thrusters, the leveraging of a state-of-the-art thrust allocation algorithm, and the development of both a path-following controller and a dedicated imaging system. The performance of the optimized platform is demonstrated in a simulation and in actual real sea visual survey missions.

Keywords: dynamics of underwater vehicles; hovering autonomous underwater vehicle (AUV); hydrodynamic coefficients; path following; thruster allocation; underwater imaging; visual survey



Citation: Gutnik, Y.; Avni, A.; Treibitz, T.; Groper, M.

On the Adaptation of an AUV into a Dedicated Platform for Close Range Imaging Survey Missions. *J. Mar. Sci. Eng.* **2022**, *10*, 974. <https://doi.org/10.3390/jmse10070974>

Academic Editor: Giacomo Picardi

Received: 12 June 2022

Accepted: 11 July 2022

Published: 15 July 2022

Publisher's Note: MDPI stays neutral with regard to jurisdictional claims in published maps and institutional affiliations.



Copyright: © 2022 by the authors. Licensee MDPI, Basel, Switzerland. This article is an open access article distributed under the terms and conditions of the Creative Commons Attribution (CC BY) license (<https://creativecommons.org/licenses/by/4.0/>).

1. Introduction

Visual surveys of the seabed enable us to quantify underwater benthic communities [1,2], explore archaeological sites [3], inspect sub-sea structures [4], and map the seabed [5,6]. These attributes make them extremely important tools in marine research. The underwater medium, however, presents significant challenges to imaging survey platforms. The rapid attenuation of light and the water turbidity force such platforms to operate close to the surveyed object, in particular when high-resolution data are required. Consequently, to map a large area, sets of images must be collected and stitched together into a photomosaic [7,8]. High-quality photomosaics comprise images collected under homogeneous optical conditions and depend on the amount of overlap between the images in the set [6,9]. Acquiring such an image set requires roaming the camera with high precision along the mapping transects while maintaining constant altitude and orientation.

Often, image sets are collected by scuba divers; however, divers are limited by dive time and depth. In addition, they are unable to precisely navigate long transects while maintaining their cameras at a constant orientation and altitude. The development of advanced underwater platforms such as remotely operated vehicles (ROVs) and autonomous underwater vehicles (AUVs) has allowed researchers to execute complicated missions while extending the effective time and depth, improving data quality and eliminating the inherent risks of human involvement. ROVs are generally powered and remotely controlled from surface support vessels via a tether that provides power, real-time control and video stream channels. The tether, however, limits the range and mobility of the vehicle. Furthermore, the deeper the missions are, the higher the deployment complexity is [3].

AUVs are increasingly employed in underwater missions previously performed by human divers or by ROVs. Multiple on-board sensors allow AUVs to navigate autonomously through predefined missions without the need for constant human supervision. In addition,

their untethered operation enables them to maneuver freely without the risk of tether entanglement, in particular when operated close to the seabed and in complex environments.

These features make AUVs an excellent candidate platform for underwater visual survey missions [2,10]. Consequently, dedicated imaging and lighting systems have been developed [11–13]. Methods for improving the capabilities of AUVs' during autonomous visual mapping and survey missions were also recently introduced [14,15], and new concepts of low cost AUVs for close-to-seabed and high-resolution imaging in shallow water have been proposed [16,17]. Mature AUVs are currently being employed in visual surveys of archaeological sites [18], hydrothermal vents [19], coral reefs [20] and benthic communities [21].

To collect high-quality image sets, AUVs are required to operate with high precision at low altitude. Achieving such precision is challenging, particularly in shallow waters and over rugged terrains. Hovering type AUVs are optimized for precise motion control at low speed, mainly by employing several thrusters for motion control. Such AUVs are commonly designed with an ROV-like frame such as the Hobalin AUV [19] or with multiple streamlined hulls such as the Girona 500 [22], SeaBED [2], ABE [23] and TriMARES [24]. Operation of multiple-hull-shaped AUVs, however, may be cumbersome in a vicinity adjacent to a cluttered seabed or complex objects such as shipwrecks or coral reefs.

AUVs with a single streamlined, torpedo-shaped hull, such as the Gavia [25], REMUS 600 [26], HUGIN [27], and LAUV [28], are also employed in imaging missions. Their streamlined shape provides better hydrodynamic efficiency and a small form factor that eases the operation in confined environments. To maintain their superior hydrodynamic characteristics and endurance, these AUVs are typically controlled by a single tail propeller and planes. The underactuated configuration, however, results in a coupled motion that sometimes limits the AUV's ability to accurately follow transects and to perform delicate maneuvers at slow speeds. In complex and confined environments, in particular when currents are present, these capabilities are essential for close-range imaging missions. In addition, a single hull structure is characterized by close proximity of the vehicle's center of gravity (\overline{CG}) and center of buoyancy (\overline{CB}), which results in inferior hydrostatic stability due to small restoring moments, in particular in roll and pitch. Therefore, torpedo-shaped AUVs are mainly employed for long-range and high-altitude surveys and less suitable for close to seabed imaging missions [22].

To better adapt this AUV type for close range and high-resolution imaging missions, a dedicated motion control system may be incorporated [29]. Such a system will facilitate accurate and decoupled motion control and path following along imaging transects to support high quality data collection and achieve the required amount of overlap for the generation of photomosaics.

The Hatter Department of Marine Technologies at the University of Haifa (UH) operates a SPARUS II AUV as a platform for research in the field of underwater technologies, sensors, and marine robotics. We recently proposed to develop new and enhance existing high-resolution seabed imaging survey performance capabilities as part of an Israel Ministry of National Infrastructure, Energy and Water Resources and Israel Ministry of Science, Technology and Space call. Our proposal entailed enhancing the maneuverability of the vehicle through the addition of two strategically positioned thrusters, providing sway and decoupled yaw control. A novel thruster allocation algorithm was implemented to optimize the new, over-actuated propulsion system configuration and an improved path-following controller was developed and integrated into the vehicle's control system. To study and evaluate the enhanced propulsion system, a dynamic model was developed and incorporated into a software-in-the-loop simulation. In addition, a dedicated imaging payload, consisting of stereo, downward-looking cameras, and a system of strobes was developed and integrated. Finally, the upgraded platform named "ALICE" (see Figure 1) was tested in a real underwater visual survey mission, where a substantial improvement in the vehicle's performance capabilities for this type of mission was demonstrated. This paper describes this development and improvement process.

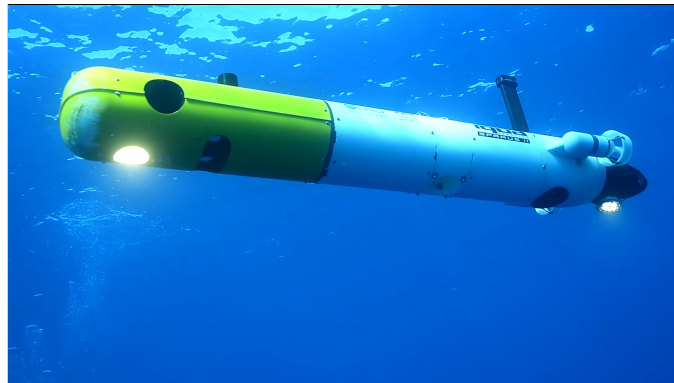


Figure 1. ALICE AUV during sea experiments in the Mediterranean sea.

The paper is organized as follows: Section 2 describes the basic configuration of the existing platform while Section 3 describes the development of a dedicated imaging payload and its integration with the SPARUS II platform. Section 4 details the requirements for high-resolution imaging survey, based on the developed imaging payload and Section 5 describes the hardware configuration of ALICE, the modified vehicle. Section 6 describes the development of a dynamic model of ALICE to facilitate performance evaluation and control system design. ALICE's motion control system, including the development of an optimized thruster allocation algorithm and improved path-following controller, are described in Section 7. Evaluation of ALICE's performance in simulation is provided in Section 8, and a demonstration of ALICE in real imaging survey missions is presented in Section 9. Conclusions are presented in Section 10.

2. The SPARUS II AUV

Our existing platform, the SPARUS II [30], is a torpedo-shaped AUV with partial hovering capabilities, developed by IQUA Robotics Inc. (<http://iquarobotics.com/>). The vehicle's operating speed is 0–2 m/s, and its maximum operating depth is 200 m. Its small dimensions (1.6 m in length and 230 mm in diameter) and low weight (approx. 52 kg) facilitate its deployment from and retrieval to relatively small support surface vessels. For underwater navigation, the vehicle is equipped with an inertial measurement unit (IMU), pressure sensors, an acoustic Doppler velocity logger (DVL), and an ultra-short baseline localization modem (USBL). The control and communication architecture is based on the COLA2, open source software architecture, implemented in the ROS environment [31]. The vehicle's payload volume can be configured to support payloads with a maximum capacity of 8 L and weight in air of 7 kg.

The original configuration of the UH SPARUS II employs three thrusters to control the AUV in three degrees of freedom (DOF). Two horizontal thrusters were mounted at the tail to control surge motion, by creating equal thrust, and yaw motion, by creating differential thrust. A single vertical tunnel thruster, located at the vehicle's center of buoyancy, controls heave motion. The sway, roll, and pitch motions are not actively controlled. Consequently, compensation for lateral drift, which may occur due to environmental disturbances, is indirectly controlled by employing the horizontal thrusters. This method, however, results in side-slip [32], causing slow and inaccurate response to unpredictable perturbations. Moreover, when the yaw motion is controlled by the horizontal thrusters, an unequal torque is created, causing an undesired roll moment.

3. Development of a Dedicated Imaging Payload

As part of the modification of the existing SPARUS II platform to enable it to provide accurate, close-to-seabed visual surveys and especially to create high-resolution (~1 mm) 3D photomosaics of the seafloor, a stereo imaging system (Figure 2) was developed. Two 9.2 megapixel Allied Vision (<https://www.alliedvision.com/>) Manta-G917 cameras were selected. To avoid distortion that may be caused by the employed flat ports [33], lenses with

a focal length of 12.5 mm were attached to the cameras, providing a field of view of 70°. The cameras were installed in two compact pressure-resistant housings that were designed in-house to fit the vehicle's payload section. Each housing consists of a camera, a flat port, and a SubCon Ethernet connector. The stereo pair was installed at a baseline of 100 mm between the cameras, which is the maximum distance the payload section supports. Two high-power LED strobes were integrated within in-house designed housings. Each strobe consists of an array of 20 Cree XHP-35 LEDs, providing 30,000 lumens at 4000 K color temperature. The strobes' beam angle was set to 120°, fully covering the camera's field of view (FOV). The cameras' housing, installed inside the vehicle's payload section, and the rear strobe, installed in the tail cone, are presented in Figure 3.

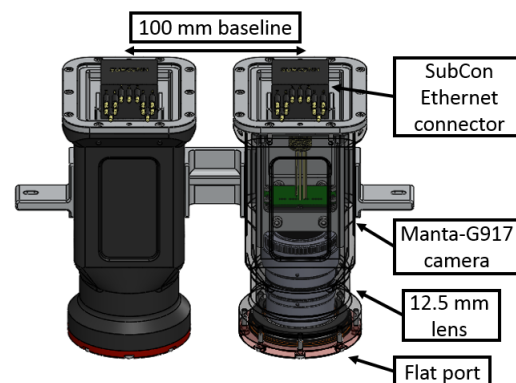


Figure 2. In-house developed stereo camera housing.



Figure 3. Stereo cameras inside the payload section (left) and rear strobe inside the tail section (right).

An Arduino based microcontroller was used to control the strobes' intensity and trigger the cameras and the strobes synchronously at a frame rate of up to 10 fps. An NVIDIA (<https://www.nvidia.com/>) Jetson TX2 GPU was employed for image acquisition, camera control, and communication with the vehicle's navigation system. Both the microcontroller and the GPU were installed inside the main hull and connected to the cameras and strobes through underwater cables and SubCon pluggable connectors.

4. Mission Planning for High-Resolution Imaging

Our survey missions are planned based on the selected imaging altitude, the cameras' parameters, and in line with the guidelines described in [13]. The direct heave control enables the SPARUS II to operate close to the seabed. Operation at low altitude, however, increases the risk of collision with obstacles on the seabed. Consequently, we conducted a series of experiments at sea, and following their results, an altitude of 2 m was determined as the optimal altitude allowing safe operation during imaging survey missions. A typical mission is defined by way-points in the commonly used "lawnmower" pattern, consisting of equally spaced one-meter straight transects that provide an overlap of 45% between two adjacent transects. To avoid motion blur, the vehicle surge speed was limited to 0.3 m/s and the camera frame rate r was set according to Equation (1) to provide an overlap of 60% along the transects (in the direction of propagation):

$$r = \frac{u}{H \cdot (100\% - O)} \quad (1)$$

where u is the surge speed, H is the altitude above the seabed, and O is the desired percentages of overlap.

Accordingly, the camera parameters were optimized to acquire images from an altitude of 2 m as follows: to avoid motion blur, the exposure period was set to 3 ms, the aperture was set to $F/4.0$ for the desired depth-of-field of 2 m, and the lenses were focused to a distance of 2 m in the water (1.5 m in the air). The camera gain was adjusted to suit the visibility conditions at the surveyed site. To determine the gain, the vehicle performed a short dive prior to the survey mission and control images were collected. Once the vehicle surfaced, the gain was evaluated and corrected accordingly.

5. Modified SPARUS II AUV—ALICE

It was found that the underactuated configuration of the SPARUS II propulsion system was insufficient for precise tracking of the imaging transects and maintaining the required overlap, particularly when currents are present and a side-slip angle is necessary to create a thrust component to compensate for drift. To improve the vehicle's capability in performing the required maneuvers, the existing propulsion system was upgraded with two Blue Robotics (<https://bluerobotics.com/>) T-200 lateral thrusters, providing direct sway control and improved yaw motion control. These thrusters were selected as a preferable choice, due to their small dimensions, competitive price, high depth rating, and sufficient thrust, as required for the performance evaluation described in Section 8.

To maximize the yaw moment, the lateral thrusters were positioned as far from the buoyancy center as possible. The forward thruster was installed inside a tunnel, in the wet payload section, while the tail thruster was installed inside a new wet tail cone section, as illustrated in Figure 4. This section was completely redesigned to accommodate the thruster and rear strobe. The thrusters' power cables were connected to dedicated drivers located in the AUV's dry pressure-resistant section through watertight SubConn Inc. (<https://www.macartney.com/what-we-offer/systems-and-products/connectors/subconn/>) connectors. The tunnel thruster configuration preserves the hull's streamlined shape, resulting in a relatively small drag penalty. In addition, this design has minimal impact on the vehicle's launch and recovery operations.



Figure 4. ALICE AUV—An autonomous platform for acquiring high-resolution 3D photomosaics. The wet payload section consists of the nose lateral thruster, the stereo cameras, and the front strobe. The tail section was redesigned to fit a second lateral thruster and the tail strobe. A GPU, LED drivers, and a microcontroller to trigger the strobes were fitted in the vehicle's dry section.

6. Dynamic Modeling for Performance Evaluation of ALICE

To facilitate design decisions and evaluate the vehicle dynamics and motion control for the required imaging missions, a detailed dynamic model and a simulated environment were developed. The model computes the vehicle's response to control forces and environmental disturbances and focuses on the vehicle's dynamics in delicate maneuvers at slow speeds.

6.1. Equations of Motion

The dynamics of the vehicle are modeled according to the generalized form of the equations of a fully submerged vehicle as specified by Fossen [34]. This form employs the *SNAME* notation in the body-fixed frame with the origin fixed at the vehicle's center of buoyancy, the x -axis extending along the hull axis of symmetry directing toward the nose, the y -axis directing toward the starboard side, and the z -axis directing downwards. The Earth-fixed frame employs the North–East–Down (NED) convention to describe the vehicle's trajectory and orientation, as illustrated in Figure 5. The relation between the body-fixed and the Earth-fixed frames is given by:

$$\dot{\eta} = J(\eta)\vec{v} \tag{2}$$

where $\eta = [x, y, z, \psi, \theta, \phi]^T$ represents the generalized position and orientation of the vehicle with respect to the Earth-fixed frame, $v = [u, v, w, p, q, r]^T$ represents the linear and angular velocities in the body-fixed frame and $J(\eta) = [J_1, J_2]^T$ is the transformation matrix between the body-fixed and Earth-fixed frames.

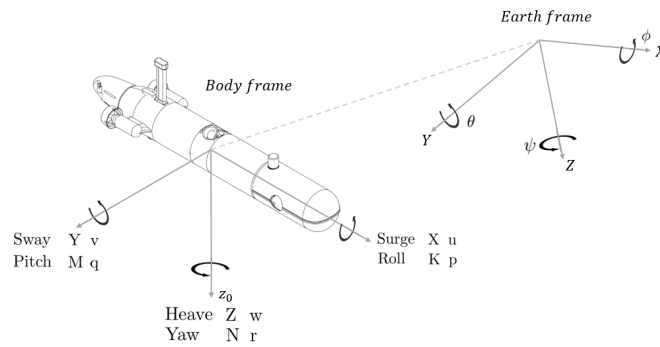


Figure 5. Body-fixed and Earth-fixed reference frames.

The sea currents are measured in the Earth-fixed frame. Assuming irrotational flow, the sea current vector is defined by $\vec{v}_c = [u_c, v_c, w_c, 0_{1 \times 3}]^T$ and transformed to the body-fixed frame by:

$$\vec{v}_c^b = J_1(\eta)\vec{v}_c \tag{3}$$

Thus, we define the relative velocity vector as:

$$\vec{v}_r = \vec{v} - \vec{v}_c^b \tag{4}$$

Under the assumption that the change in the current's velocity vector is negligible, such that $\dot{v}_c = 0$, the nonlinear equations of motion in the body-fixed frame are expressed by:

$$M\dot{\vec{v}} + C(\vec{v}_r)\vec{v}_r + D(\vec{v}_r)\vec{v}_r + \vec{g}(\eta) = \vec{\tau}_c \tag{5}$$

where M is the system inertia matrix (sum of the rigid body system inertia matrix M_{RB} ; the added mass M_A matrix); $C(\vec{v})$ is the Coriolis/centripetal matrix consisting of the rigid body matrix $C_{RB}(\vec{v})$; the added mass matrix $C_A(\vec{v})$; $D(\vec{v})$ is the hydrodynamic damping matrix combining the nonlinear damping matrix and the body lift matrix; $\vec{g}(\eta)$ is the hydrostatic restoring forces and moments vector; and $\vec{\tau}_c = [X, Y, Z, K, M, N]^T$ is the control forces vector acting on the vehicle's DOF.

6.2. Modeling of ALICE's Propulsion System

The control forces vector $\vec{\tau}_c$ combines the thrusters' open water performance, the effect of the interaction between the thrusters and the hull, and the thrusters' configuration

matrix, which defines the contribution of each thruster to the control forces vector. The axial (thrust) force T and torque Q created by a thruster’s propeller are defined by [35]:

$$T = \rho D^4 k_t n |n| \tag{6}$$

$$Q = \rho D^5 k_q n |n| \tag{7}$$

where D is the propeller diameter, n is the rotational speed, and $k_t(J)$ and $k_q(J)$ are the thrust and torque coefficients, respectively, for a specific advance ratio J . The thrust and torque coefficients were estimated using the experimental data presented in [35,36] and employing results from bollard pull experiments provided by the manufacturer.

6.2.1. Interactions between the Tunnel Thrusters and the Hull

Tunnel thrusters are considered jet producing devices. When the vehicle moves, the flow around the hull deflects the jet, creating a low-pressure area [37] as illustrated in Figure 6. As a result, due to the offset between the center of the low-pressure area and the thruster axis, the net thrust is reduced and a moment is created. Assuming the frictional effects due to the interactions between the jet and the tunnel are negligible and considering the effects of the jet deflection, the thrust created by the tunnel thrusters is expressed by [37]:

$$T = \rho D^4 k_t e^{-C(\frac{u}{u_j})^2} n |n| \tag{8}$$

where C is a thrust deduction factor and u_j is the jet speed, given by:

$$u_j = \sqrt{\frac{T_0}{\rho A_{th}}} \tag{9}$$

where T_0 is the open water thrust as given by Equation (6) and A_{th} is the cross-section area of the tunnel.

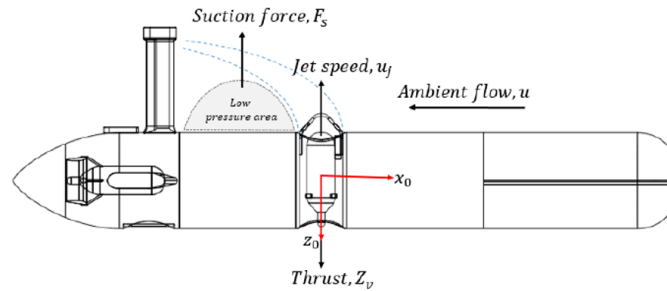


Figure 6. Interaction between the jet of the vertical tunnel thruster and the ambient flow.

6.2.2. Thruster Configuration Matrix

The contribution of each of ALICE’s thrusters to the control force vector, $\vec{\tau}_c$, is defined by:

$$\vec{\tau}_c = B \vec{f}_{th} \tag{10}$$

where $\vec{f}_{th} = [T_{th1}, T_{th2}, T_{th3}, T_{th4}, T_{th5}]^T \in \mathbb{R}^n$ is a column vector, representing the thrust created by each thruster and $B \in \mathbb{R}^{6 \times 5}$ is the thruster configuration matrix, given by:

$$B = \begin{pmatrix} 1 & 1 & 0 & 0 & 0 \\ 0 & 0 & 0 & 1 & 1 \\ 0 & 0 & 1 & 0 & 0 \\ 0 & 0 & 0 & 0 & 0 \\ 0 & 0 & 0 & 0 & 0 \\ y_{th1} & -y_{th2} & 0 & x_{th4} & x_{th5} \end{pmatrix} \tag{11}$$

where the distances y_{th1} , y_{th2} , x_{th4} , x_{th5} are measured from the vehicle's center of buoyancy to the thrusters' center of action.

6.3. Identification of the Hydrodynamic Coefficients

The hydrodynamic forces and moments acting on the vehicle due to added mass, drag and lift are described in terms of hydrodynamic coefficients (derivatives). In this work, the vehicle's coefficients were assumed to be independent of the vehicle's speed. Considering the vehicle's appendages and cavities (i.e., mast, external thrusters, camera window and tunnel thrusters), estimating these coefficients by commonly used semi-analytical and empirical methods, such as employed by Fossen [34] and presented by Horner [38,39], may be insufficient as these methods mainly approximate the vehicle's components to basic shapes and neglect interactions between components [40–42].

Computational fluid dynamics (CFD) methods are able to provide better estimation of the hydrodynamic coefficients; however, their results may be unsatisfactory due to the difficulty in modeling the smoothness of the vehicle's surface and the interaction of the propulsion system with the hull [43]. Therefore, as the actual vehicle was available, to achieve a better estimation, the vehicle's major coefficients were derived from experimental data while only derivatives that were difficult to obtain were estimated by semi-analytical or pure empirical forms.

We were unable to conduct dedicated tank tests for the purposes of this study. Consequently, hydrodynamic coefficients were estimated using data from experiments conducted at sea.

ALICE underwent dedicated sea trials off the coast of Sdot Yam, Achziv, and Haifa Bay. To minimize the possible influence of sea currents, the trials were conducted in a confined area and only in an extremely calm sea state. In addition, the vehicle's mission was defined as straight segments in different headings to allow the deduction of sea current out of the measured velocities.

The vehicle's motion during these trials was measured by the on-board sensors, where vehicle $[u, v, w]$ and sea current $[u_c, v_c, w_c]$ velocities were measured by Doppler Velocity Log (DVL). The angular rates $[p, q, r]$ were assessed by an inertial measurement unit (IMU) and the angles $[\psi, \theta, \phi]$ were computed by the vehicle's angle estimator algorithm. The vehicle's depth was measured by the pressure sensor. For the extraction of the hydrodynamic coefficients, a hybrid approach (vehicle—dynamic model) was employed. The real-time vehicle thrusters' RPM commands as recorded in the sea trials were fed as input to Equation (12) and the obtained solutions (i.e., computed trajectories) were compared with the real ones as recorded during the sea trials.

The computation of the hydrodynamic coefficients was performed in a decoupled fashion (i.e., vertical and horizontal planes) employing the following maneuvers:

1. Forward motion at various surge speeds to determine $X_{\dot{u}}$ and $X_{u|u}$;
2. Vertical ascent/descent at a constant heave speed to determine $Z_{\dot{w}}$ and $Z_{w|w}$;
3. Horizontal turns, performed by the horizontal thrusters, to determine $N_{\dot{r}}$ and $N_{r|r}$.

To differentiate the thruster-produced forces from the hydrodynamic forces in the calibration process, the thrust coefficients (and thus the thruster-produced forces) were initially calibrated according to Bollard pull test results while the hydrodynamic coefficients were adjusted to fit the vehicle's measured response in each of the listed maneuvers.

In particular, first the hydrodynamic damping coefficients were identified by manual and iterative adjustment of the related coefficients until the velocities, computed by the model, corresponded with the measured velocities. Then, the added mass coefficients were determined by adjusting the related coefficients until the computed and measured accelerations matched.

A list of the calibrated coefficients is presented in Table 1 and a comparison between the recorded vehicle's dynamics and the results of the simulation, employing identical control inputs, is presented in Figure 7.

Table 1. ALICE hydrodynamic coefficients.

Coefficient	Value	Coefficient	Value
$X_{\dot{u}}$	-28.06	$X_{u u }$	-15.23
$Y_{\dot{v}}$	-23.53	$Y_{v v }$	-321.59
$Z_{\dot{w}}$	-27.81	$Z_{w w }$	-326.16
$K_{\dot{p}}$	-0.04	$K_{v v }$	-3.4
$M_{\dot{q}}$	-10.48	$K_{p p }$	-0.19
$M_{\dot{w}}$	-5.6	$M_{q q }$	-180
$N_{\dot{r}}$	-11.26	$M_{z w }$	26.63
$N_{\dot{v}}$	-8.53	$M_{u u }$	0.14
Z_{uw}	-39.7	$N_{r r }$	-54.1
M_{uw}	-8.49	$N_{v v }$	-1.95

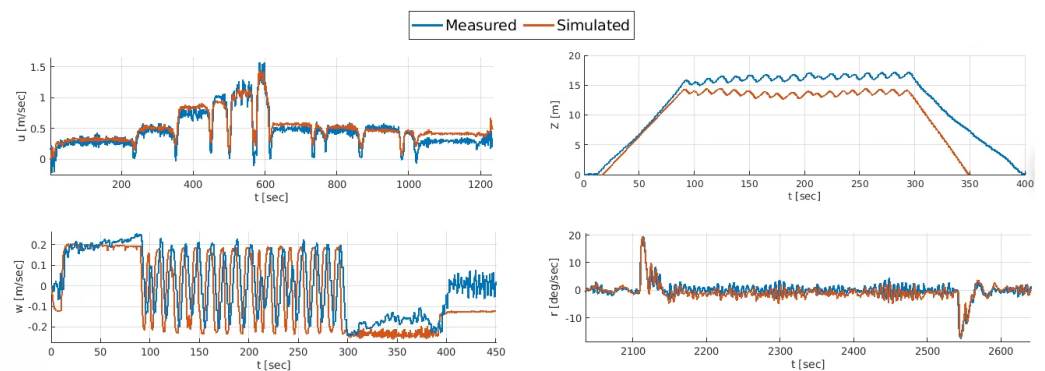


Figure 7. Model calibration results for surge (top left), heave (bottom left), depth (top right) and yaw rate (bottom right) as determined by the experiments.

A second data set was used for the validation of the calibrated model. The data set was recorded during navigation between way-points in a lawn mower pattern at a surge velocity of 0.2 m/s and depth of 2 m. Comparison between the solution of the calibrated model and the measured dynamics, as presented in Figure 8, shows good agreement and suggests successful calibration of the dynamic model.

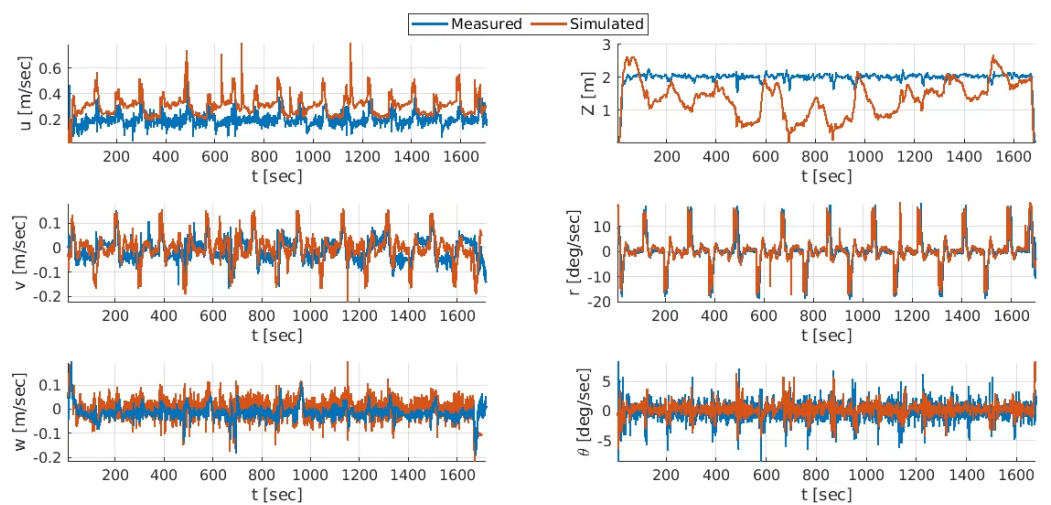


Figure 8. Comparison between the vehicle’s dynamic response, as computed by the calibrated model and the actual response, as measured at sea for surge (top left), sway (middle left), heave (bottom left), depth (top right), yaw rate (middle right) and pitch (bottom right).

The developed dynamic model was then employed when fine-tuning ALICE’s control system. This allowed ALICE to perform the required precise imaging survey missions.

6.4. Numerical Implementation of the Dynamic Model

The differential equations of motion, presented in Equation (5), are highly nonlinear and coupled. To compute the acceleration, velocity, and orientation of the vehicle, Equation (5) was rearranged:

$$\dot{\vec{v}}_{(t)} = M^{-1} [\vec{\tau}_{c(t)} - C(\vec{v}_{(t)})\vec{v}_{(t)} - D(\vec{v}_{(t)})\vec{v}_{(t)} - \vec{g}(\vec{\eta}_{(t)})] \tag{12}$$

and implemented in the MATLAB-SIMULINK (<https://www.mathworks.com/products/simulink.html>) environment, solving $\dot{\vec{v}}, \vec{v}$ for the input τ_c , where \vec{v} is solved by numeric integration of $\dot{\vec{v}}$ and the vehicle’s trajectory and orientation, referenced to the Earth-fixed frame, $\vec{\eta}$ are obtained by numeric integration of Equation (2).

7. AUV Motion Control System

The ALICE control architecture consists of a three-level control hierarchy. The top-level controllers compute the required position and orientation of the vehicle according to the required behavior: (1) Keep Position controller for anchoring and station keeping, (2) Go-To controller for reaching a specific point and (3) Line-of-Sight (LOS) controller for following a straight path. The output of the top-level controller consists of a set of decoupled position and velocity requests in surge, sway, heave, and yaw. An inner loop employs a PID controller for each DOF to compute the required forces and moments in each direction to achieve the desired position and velocities. A low-level controller is used to allocate the required forces and moments to a specific thruster, and the thruster’s set-point is computed by a force to set-point mapping.

With its upgraded configuration, ALICE’s sway motion could now be directly controlled by the additional lateral thrusters while the yaw motion has become over-actuated DOF since it can be controlled by both the horizontal and the lateral thrusters. These upgraded motion control capabilities were realized in the development of the upgraded thruster allocation algorithm and an improved path-following controller.

The dynamic model, described in Section 6, was used to optimize both the low-level and the top-level controllers’ parameters to achieve the desired performance for close range imaging missions, as described in Section 4.

7.1. Upgraded Thruster Allocation Algorithm

Since ALICE’s yaw motion is an over-actuated DOF, the thrust distribution for yaw motion control can be optimized to reduce power consumption, achieve desired dynamic response, and facilitate redundancy in case of thruster failure. Considering Equation (8), at high surge speeds, where the efficiency of the lateral thrusters is low, the horizontal thrusters are preferred over the lateral thrusters. At slow speeds, however, and, in particular, during imaging surveys, the torque produced by the horizontal thrusters may cause undesired roll motions. Therefore, in this scenario, the lateral thrusters are preferred. To optimize the thrust distribution according to this logic, the redistributed pseudo-inverse (RPI) method [44,45] was implemented, solving \vec{f}_{th} by iterative computation of Equation (13):

$$\vec{f}_{th} = -c + W^{-1}B^T [BW^{-1}B^T + \epsilon I_3]^{-1} [\vec{\tau}_c + B_0c] \tag{13}$$

where B_0 is the unconstrained allocation matrix (11), B is initialized with B_0 and updated according to the thrusters’ availability, c is initialized with zeros and updated according to the thrusters’ saturation, and I_3 is an identity matrix. ϵ is a small regularization parameter defined to avoid singularity in the RPI expression when B does not possess full rank and W is a weighting matrix.

To optimize the vehicle’s stability in roll when operating at low speeds, the weights of the lateral and horizontal thrusters in W are dynamically updated according to the measured roll angles ϕ :

$$W = \begin{pmatrix} w_1(\phi) & 0 & 0 & 0 & 0 \\ 0 & w_2(\phi) & 0 & 0 & 0 \\ 0 & 0 & 1 & 0 & 0 \\ 0 & 0 & 0 & w_4(\phi) & 0 \\ 0 & 0 & 0 & 0 & w_5(\phi) \end{pmatrix} \tag{14}$$

where $w_{1,2}$ are the weights of the lateral thrusters and $w_{4,5}$ are the weights of the horizontal thrusters, defined as follows:

$$w_{1,2} = \min \left[\frac{|\phi|}{\phi_{max}}, 1 \right] \tag{15}$$

$$w_{4,5} = 1 - w_{1,2} \tag{16}$$

The implemented RPI method with real-time reconfigurable weighing matrix is summarized in Algorithm 1.

Algorithm 1: RPI method with dynamic weighting matrix.

Data: $B_0, \vec{\tau}_c$, Roll angle (ϕ), Thrusters saturation vector (\vec{f}_{max})

Result: \vec{f}_{th}

$B \leftarrow B_0$;

$\vec{c} \leftarrow [0, 0, 0, 0, 0]$;

$W(\phi) \leftarrow \phi$;

while ($i < \text{max iterations}$) **do**

$\vec{f}_{th} = -c + W^{-1}B^T [BW^{-1}B^T + \epsilon I_3]^{-1} [\vec{\tau}_c + B_0c]$;

if $\vec{f}_{max}[n] < \vec{f}_{th}[n]$ **then**

$\vec{c}[n] \leftarrow -\vec{f}_{max}[n]$;

$B[:,n] \leftarrow 0$;

else

Return \vec{f}_{th}

end

$i++$

end

7.2. Improved Path-Following Controller

The under-actuated original configuration of the SPARUS II AUV employed the popular LOS controller [46] to follow a straight path, created by way-points. The controller computes the required heading toward an interception with a moving point on the track:

$$\psi_{LOS} = \tan^{-1} \left(\frac{Y_{LOS} - Y_o}{X_{LOS} - X_o} \right) \tag{17}$$

where (X_o, Y_o) are the vehicle’s coordinates and (X_{LOS}, Y_{LOS}) are the coordinates of the moving point of interception determined by the look-ahead distance, Δh , as illustrated in Figure 9. Ideally, the cross-track error e will converge to zero and the vehicle’s heading will converge to the direction of the path β . When lateral disturbances such as cross-current are present, lateral drift is avoided by steering the vehicle at a side-slip angle. This method, however, results in an undesired heading and may result in poor path following due to slow response by the indirect motion control. This behavior impairs the vehicle’s capability to accurately follow the imaging transects.

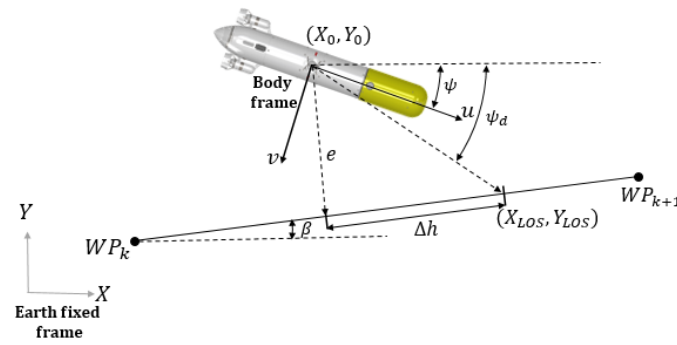


Figure 9. LOS controller geometry.

With ALICE’s upgraded configuration, the additional thrusters are able to counter drift, thus addressing lateral disturbances effectively, and eliminating the need to crawl at a side-slip angle. This allows the heading aligned with the direction of the path to be maintained, thereby improving the accuracy of the path following during the required mission.

The sway motion control is incorporated into the LOS controller to eliminate the lateral component of the cross-track error e_v , defined by:

$$e_v = e \cdot \cos(\beta - \psi) \tag{18}$$

A PID controller is designed to control the sway motion as follows:

$$v_{req} = k_P \cdot e_v + k_I \cdot \int e_v dt + k_D \cdot \dot{v} \tag{19}$$

where k_P , k_I , and k_D are, respectively, the proportional, integral, and derivative gains. Initially, the gains were fine-tuned according to the response of the modeled vehicle in a simulated mission with simulated currents, as described in detail in Section 8. Later, the gains were adjusted according to the vehicle’s behavior during sea experiments, described in Section 9. The sway motion is, however, considered inefficient due to the vehicle’s high lateral drag compared to the axial drag dominating the surge motion. Therefore, a switching strategy between the classic, heading control law and the proposed sway motion controller is implemented such that, for a small cross-track error, the vehicle follows the path laid out by the sway controller presented in Equation (19) and maintains the path direction ($\psi_{req} = \beta$). For a large cross-track error, the vehicle will converge to the path dictated by the heading control law as presented in Equation (17).

8. Software-in-the-Loop Simulation for ALICE’s Performance Evaluation

The vehicle’s ability to accurately perform imaging survey missions was evaluated by employing software-in-the-loop simulation implemented in the COLA2 architecture, provided by IQUA Robotics. This simulation allows the vehicle’s control and navigation software to be tested while simulating the vehicle’s sensors and dynamics. To match the upgraded vehicle configuration and improve the simulation results, the existing simulation was modified using the dynamic model described in Section 6 with the obtained hydrodynamic coefficients, described in Section 6.3.

To begin with, the simulation was used to calibrate the PID gains of the modified LOS controller (Equation (19)). These gains were calibrated according to the dynamic response of the simulated vehicle during motion along two, opposite in direction, transects that were defined by four way-points.

To investigate the effect of uncertainties of the hydrodynamic coefficients and external disturbances on the AUV’s performance, the obtained hydrodynamic coefficients, associated with motion in the horizontal plane, were altered and different sea currents were applied as follows:

1. The added mass terms $X_{\dot{u}}$, $Y_{\dot{v}}$ and $N_{\dot{r}}$ were multiplied by a factor of 0.5 and 2 (see Figures 10 and 11);
2. The hydrodynamic damping terms $X_{u|u|}$, $Y_{v|v|}$ and $N_{r|r|}$ were multiplied by a factor of 0.5 and 2 (see Figures 12 and 13);
3. Simulated cross-current of 0.1, 0.2, 0.25 m/s were applied (see Figures 14–16).

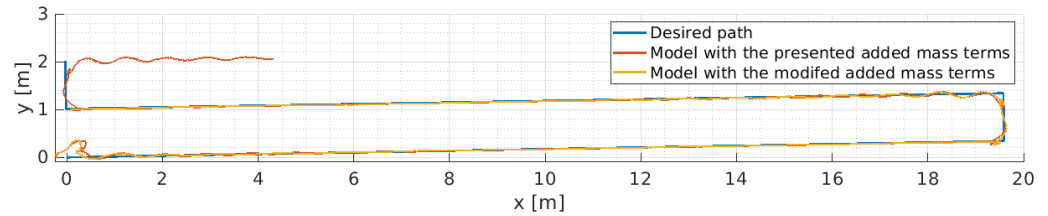


Figure 10. Simulation results for path following employing the modified controller with added mass terms multiplied by a factor of 0.5.

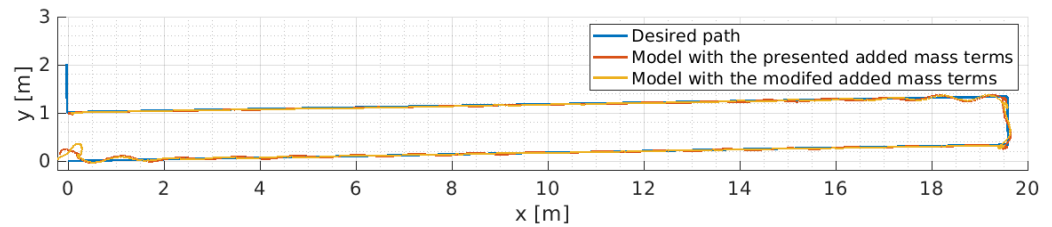


Figure 11. Simulation results for path following employing the modified controller with added mass terms multiplied by a factor of 2.

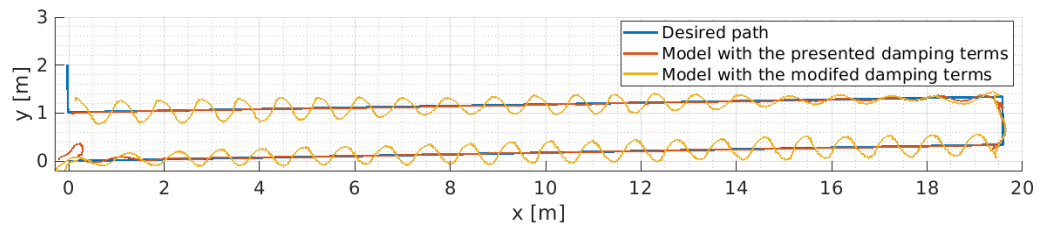


Figure 12. Simulation results for path following employing the modified controller with hydrodynamic damping terms multiplied by a factor of 0.5.

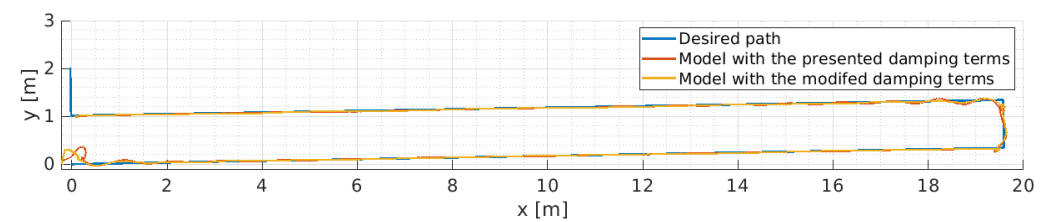


Figure 13. Simulation results for path following employing the modified controller with hydrodynamic damping terms multiplied by a factor of 2.

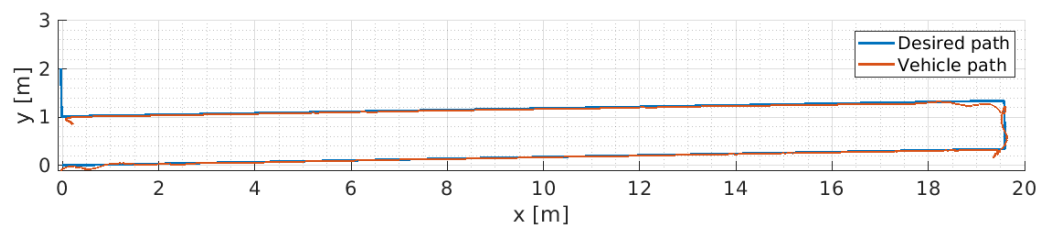


Figure 14. Simulation results for path following employing the modified controller with cross-current of 0.1 m/s.

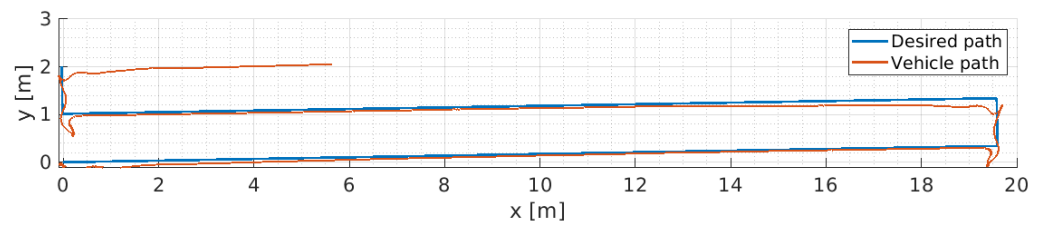


Figure 15. Simulation results for path following employing the modified controller with cross-current of 0.2 m/s.

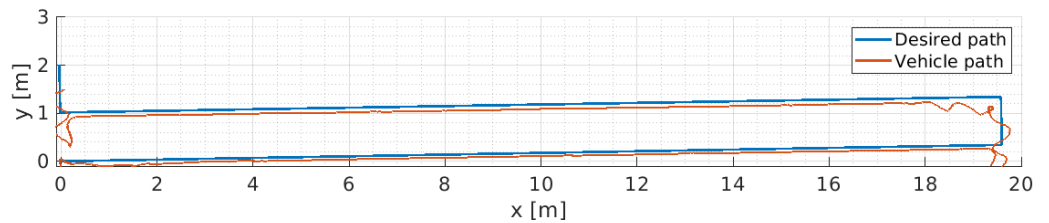


Figure 16. Simulation results for path following employing the modified controller with cross-current of 0.25 m/s.

The results of the simulations suggest that the proposed controller is able to compensate for a relatively high uncertainty in the hydrodynamic coefficients and for cross-currents up to 0.25 m/s.

Following the completion of the fine-tuning process, the simulation was used to test the vehicle’s control system in a complete sequence of an imaging survey mission. The mission was defined according to the requirements described in Section 4 by designating way-points to create 22 equidistant straight transects at one-meter intervals. The vehicle’s velocity along the transects was set to 0.25 m/s and a sea current of 0.1 m/s with the direction perpendicular to the transects (cross-current) was defined to simulate real sea conditions.

To compare the modified vehicle’s configuration to the original one, the mission was first performed by simulating the original configuration (SPARUS II), which employs 3DOF motion control and the basic LOS path-following controller. The results of the computed path (Figure 17, left), the cross-track error (Figure 18), and the heading error, as measured between the vehicle’s heading and the direction of the path (Figure 19), illustrate the inability of the original configuration to perform such accurate path following under real sea conditions, where a cross-track error of about 0.5 m and a heading error (due to side-slip) of 20° were computed.

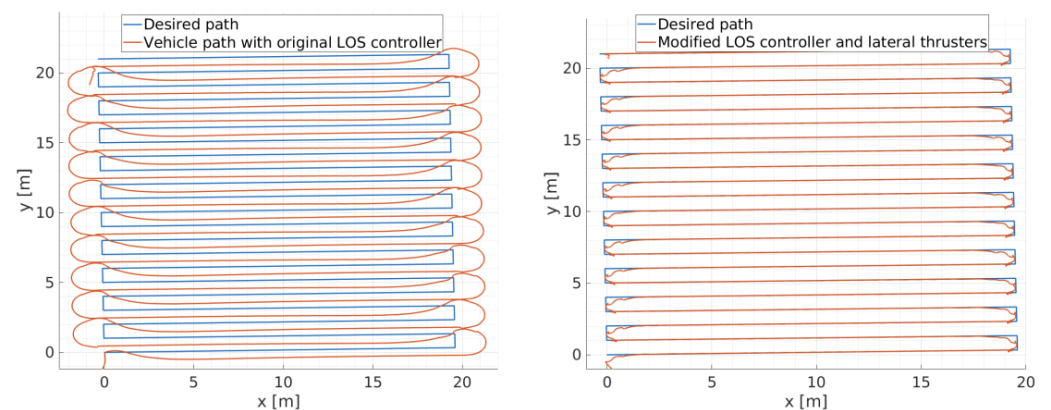


Figure 17. Simulation results for a lawn mower pattern employing the vehicle’s original configuration—SPARUS II (left) and the modified configuration—ALICE (right).

The modified configuration of the vehicle (ALICE), consisting of the two additional tunnel thrusters, the optimized thruster allocation described in Section 7.1, and the improved path-following controller discussed in Section 7.2, were incorporated into the COLA 2 architecture and tested by performing the defined mission in the software-in-the-loop simulation.

The computed path (Figure 17, right), the cross-track error (Figure 18), and the heading error (Figure 19) show a significant improvement in the vehicle’s ability to accurately follow the desired path, where a cross-track error of less than 1 cm and heading error of 1° were obtained, implying that the ALICE configuration improves the vehicle’s ability to perform the required imaging missions.

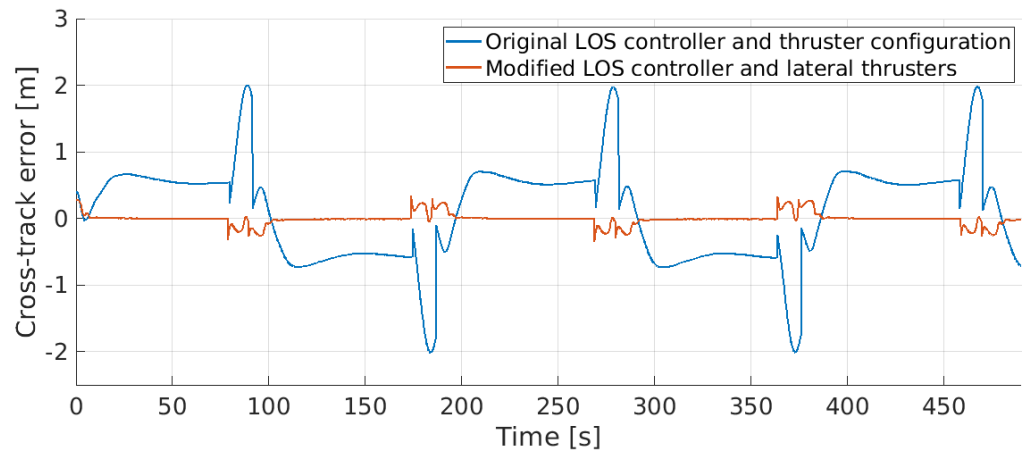


Figure 18. Simulation results for cross-track error during lawn mower pattern path following employing the vehicle’s original configuration—SPARUS II and the modified configuration—ALICE.

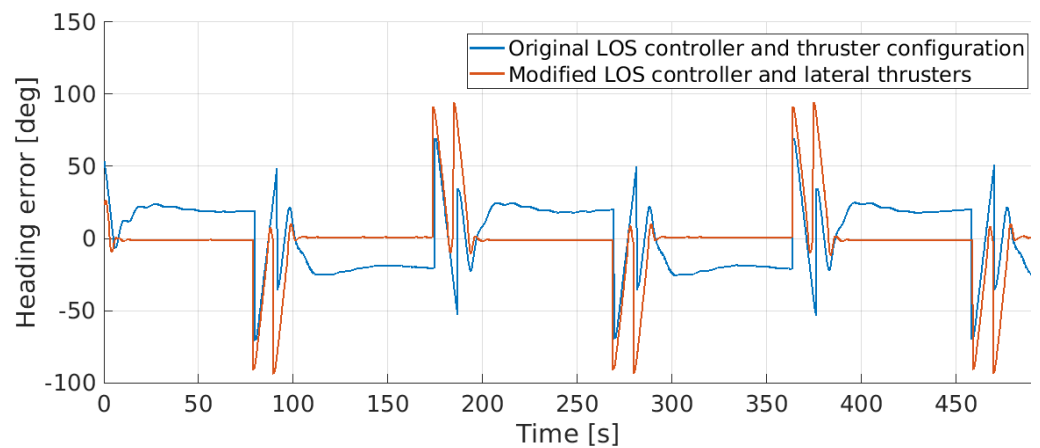


Figure 19. Simulation results for heading error during lawn mower pattern path following employing the vehicle’s original configuration—SPARUS II and the modified configuration—ALICE.

9. Real Sea Experiments and Discussion

The performance of ALICE was evaluated in real sea experiments. To begin with, an experiment was conducted to test the upgraded path-following controller and fine-tune the controller’s gains. The test mission was defined by equidistant straight transects at two-meter intervals and constant depth. To evaluate the upgraded controller, the mission was repeated twice. First, with the ALICE configuration and upon completion of the first mission, its architecture was switched back to the original SPARUS II configuration. The vehicle’s position and orientation during the experiments were recorded and processed to determine the cross-track error and heading error. The recorded path of ALICE is presented in Figure 20, the cross-track error in Figure 21, and the heading error in Figure 22. The

recorded path of the SPARUS II configuration is presented in Figure 23, the cross-track error in Figure 24, and the heading error in Figure 25.

The results of the experiment performed with ALICE present small cross-track (~ 0.1 m) and heading ($\sim 5^\circ$) errors in addition to fast convergence to the path while the SPARUS II configuration presents high cross-track (~ 0.4 m) and heading ($\sim 10^\circ$) errors as well as slow convergence to the path.

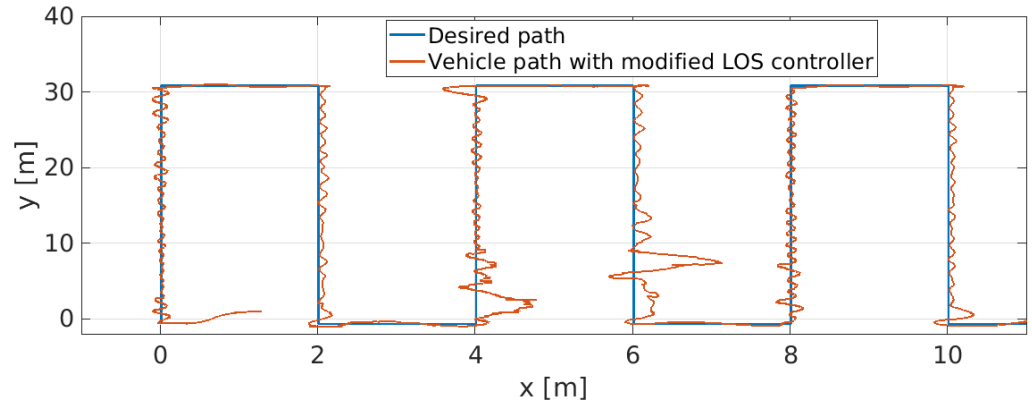


Figure 20. Vehicle’s path, employing the ALICE configuration along the test mission

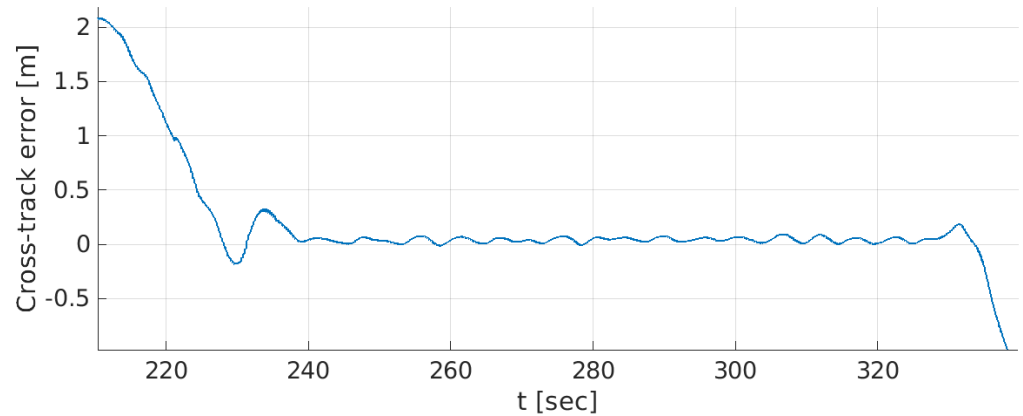


Figure 21. Cross-track error, employing the ALICE configuration along a single transect.

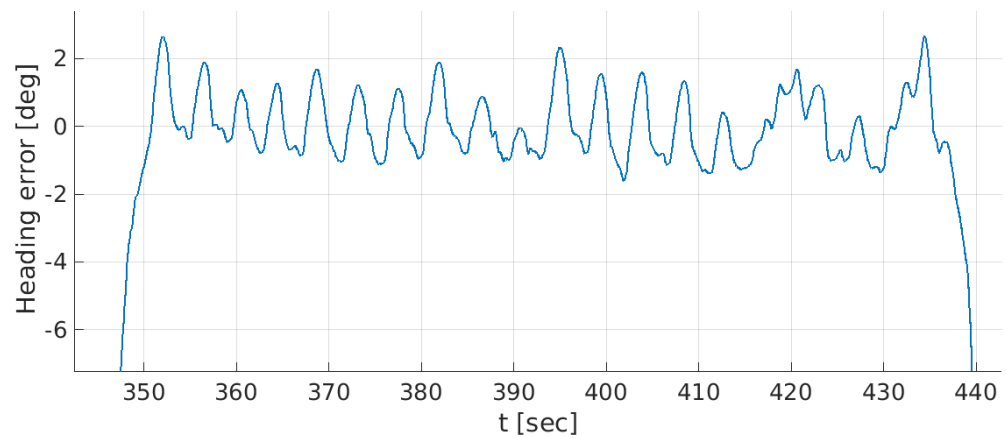


Figure 22. Heading error, employing the ALICE configuration along a single transect.

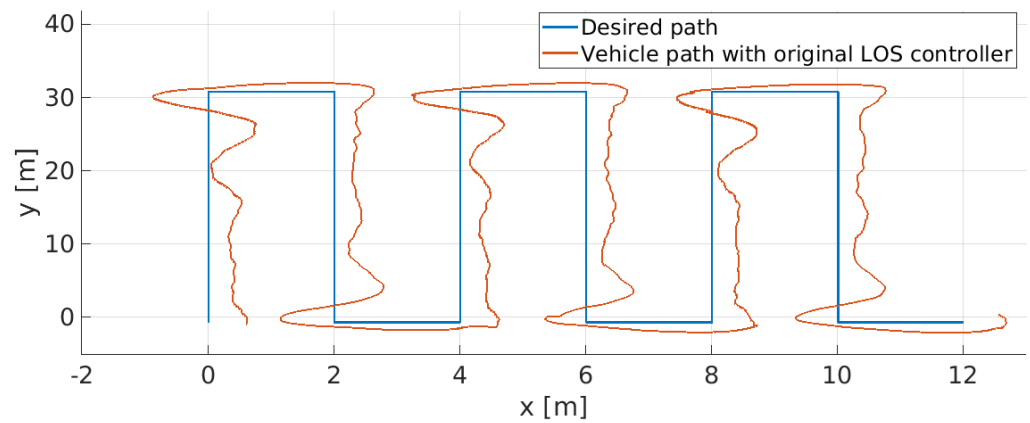


Figure 23. Vehicle’s path, employing the SPARUS II configuration along the test mission.

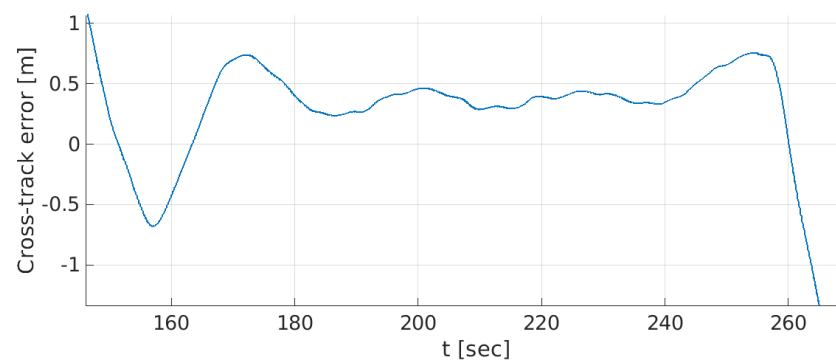


Figure 24. Cross-track error, employing the SPARUS II configuration along a single transect.

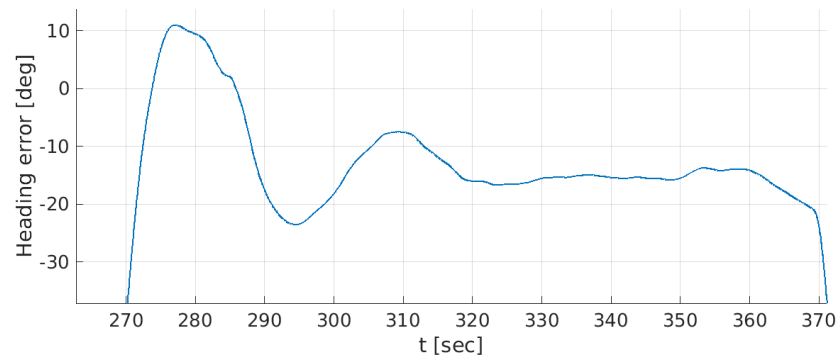


Figure 25. Heading error, employing the SPARUS II configuration along a single transect.

Following the test mission, ALICE was tested in an actual imaging survey mission that was conducted over Israel’s Mediterranean Sea seabed in a coastal area near Achziv at an altitude of 2 m above the seabed. The mission was defined as surveying an area of 15 m to 17 m around a part of a shipwreck. As was done in the first experiment, the mission was repeated with the ALICE and the SPARUS II.

The recorded path (Figure 26, left) and heading (Figure 27) of the SPARUS II configuration present slow convergence to the path with a mean cross-track error of 0.36 m. This result demonstrates the inability of this configuration to follow the targeted path with the desired precision while maintaining the heading aligned with the direction of the path. With the ALICE configuration, the recorded path (Figure 26, center) and heading (Figure 28) demonstrate precise path following along the imaging transects with a mean cross-track error of 0.12 m. In addition, a comparison between the vehicle’s roll angles as recorded with the SPARUS II configuration (Figure 29) to the roll angles as recorded with the ALICE configuration (Figure 30) shows an improvement in the roll stability where the roll angles during the horizontal turns decreased from 20–30° to less than 10°.

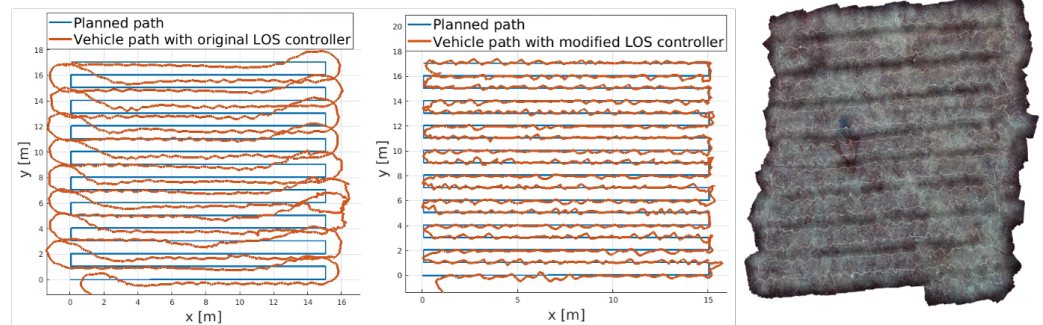


Figure 26. (Left) Vehicle’s path, employing the SPARUS II configuration along a survey mission; (Center) Vehicle’s path, employing the ALICE configuration along a survey mission; (Right) Actual path calculated from camera positions on top of the generated mosaic.

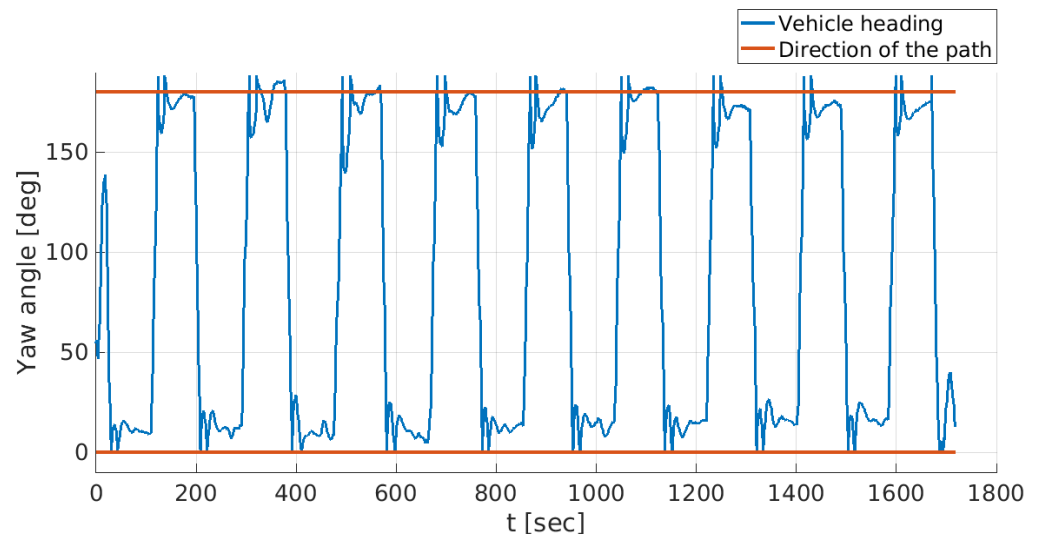


Figure 27. Vehicle’s heading during the mission, employing the SPARUS II configuration. The direction of the survey transects was defined from/to North to/from South (0–180).

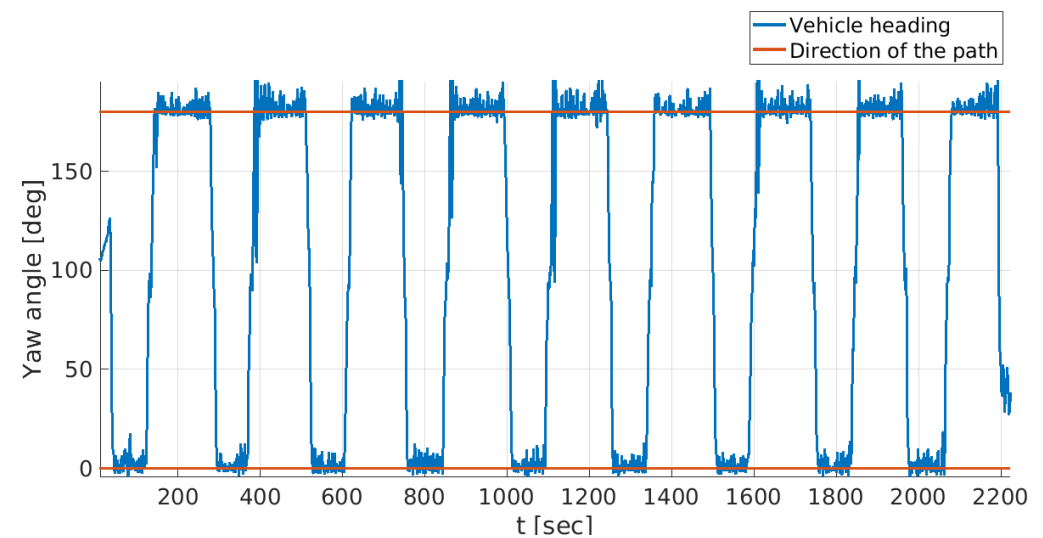


Figure 28. Vehicle’s heading during the mission, employing the ALICE configuration. The direction of the survey transects was defined from/to North to/from South (0–180).

The results of the test and the survey missions suggest that the ALICE configuration significantly enhances the vehicle's capability to follow imaging transects with high precision while maintaining heading alignment with the direction of the path and maintaining small roll angles during the transition between transects. It produced improved overlap between data sets and maintained a homogeneous perspective throughout the mission, thus improving the quality of the data collected.

The data collected with ALICE was processed using the Agisoft Metashape (<https://www.agisoft.com/>) commercial 3D photogrammetry software to produce large-scale mosaics (Figure 26, right and Figure 31) and a reconstructed 3D model of the shipwreck (Figure 32). The vehicle path, as computed by the software, is marked by white dots in Figure 31, providing additional validation of the path-following accuracy.

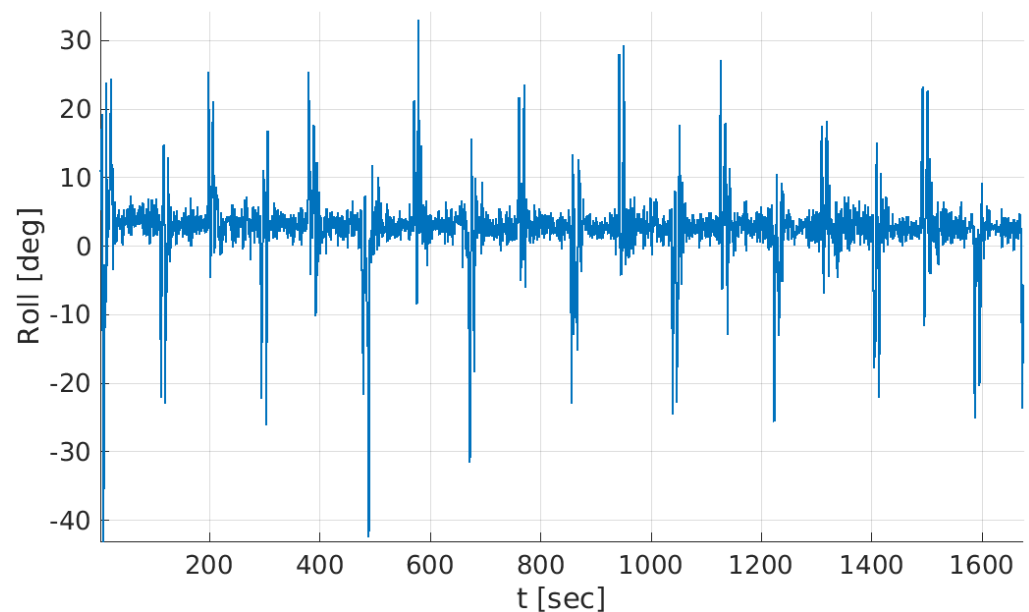


Figure 29. Vehicle's roll angle during the mission, employing the SPARUS II configuration. The "spikes" are the moments of turns.

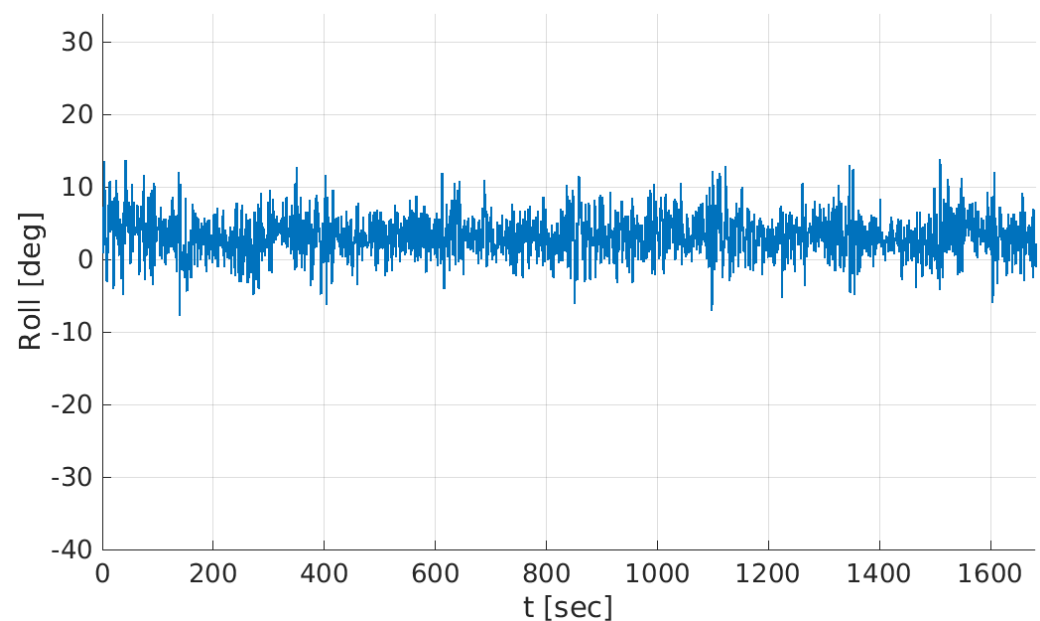


Figure 30. Vehicle's rollangle during the mission, employing the ALICE configuration.

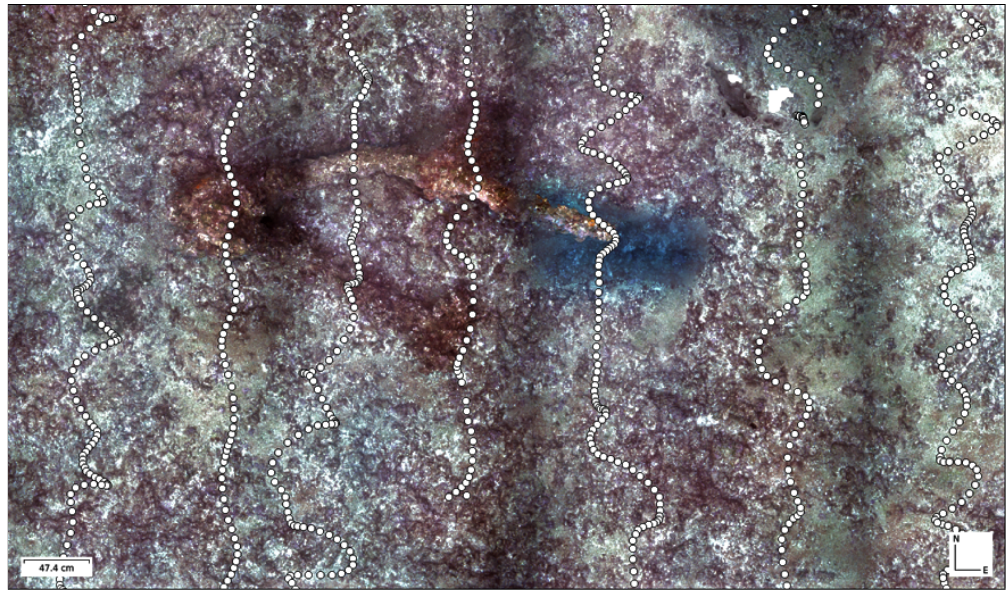


Figure 31. Close-up of the mosaic in Figure 26, right, acquired at Achziv, along the northern section of Israel's Mediterranean coast. It depicts a part of a shipwreck lying a rocky reef. The AUV's path is depicted using white dots.



Figure 32. Different viewpoint of the 3D reconstruction of the shipwreck shown in Figure 31.

Finally, ALICE was employed in an additional seabed survey mission as part of a collaboration with the marine division of the Israel Antiquities Authority with the goal of surveying and reconstructing the submerged ancient harbor of Caesarea. The survey area was selected to be an area of 10 m to 30 m at 8 m depth around an ancient dock. The survey was performed at an altitude of 3 m to provide additional safety margins due to large rocks and unstructured seabed at the site. ALICE's ability to collect high-resolution images and to provide the necessary data for precise 3D reconstruction is also demonstrated by the results of these surveys, which are shown in Figure 33.

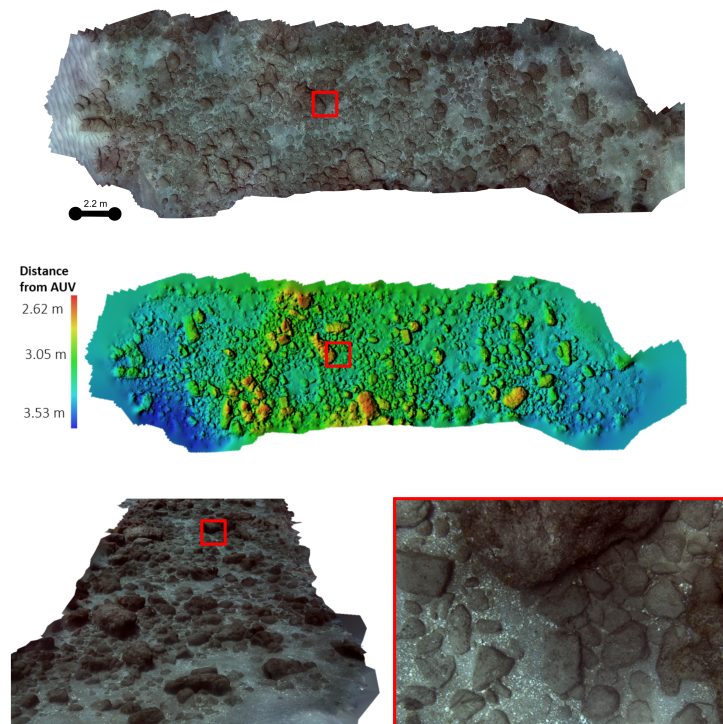


Figure 33. 3D mosaic of a Roman underwater harbor, in Caesarea, Israel. (**Top**) Mosaic of an area of 8 m × 27 m; (**Middle**) 3D reconstruction of the same area; (**Bottom left**) another viewpoint of the reconstructed 3D; (**Bottom right**) zoom-in of an area marked with a red rectangle in the top mosaic. Full model can be viewed in <https://sketchfab.com/3d-models/caesarea-roman-underwater-harbour-da2ca77fc6141bb8e1261fb6f1d1187>.

10. Conclusions

The present study reports modifications performed on a small-sized AUV so that it could serve as a powerful imaging platform for precise and high-resolution visual seabed mapping and inspection. Two lateral thrusters were added to enable sway and decoupled yaw control, and an imaging system, consisting of stereo cameras and strobes, was developed and integrated into the vehicle. To study the vehicle maneuverability and develop the upgraded propulsion and control systems, a dynamic model was developed and validated using experimental data in a hybrid simulation process. A dedicated thruster allocation algorithm was developed and implemented to optimize the vehicle's dynamic stability in roll and enable decoupled motion control in yaw and sway. In addition, an improved path-following algorithm was developed to increase the vehicle's ability to follow the imaging transects in real sea conditions. A comparison between the vehicle's original configuration and the modified configuration demonstrates the improved performance. Finally, the abilities of the modified AUV, ALICE, were successfully demonstrated during a series of missions at sea, where imaging data were collected and then processed into 3D photomosaics.

Author Contributions: The contribution of each author is specified as follows: Conceptualization, Y.G., M.G., and T.T.; methodology, Y.G. and M.G.; software, Y.G.; validation, Y.G. and A.A.; writing—original draft preparation, Y.G. and A.A.; writing—review and editing, M.G. and T.T.; visualization, Y.G. and A.A.; supervision, M.G. All authors have read and agreed to the published version of the manuscript.

Funding: This research was funded by the Leona M. and Harry B. Helmsley Charitable Trust, the Maurice Hatter Foundation, the Murray Foundation, the Israel Ministry of National Infrastructures, Energy and Water Resources Grant No. 218-17-008, and the Israel Ministry of Science, Technology and Space Grant No. 3-12487.

Institutional Review Board Statement: Not applicable.

Informed Consent Statement: Not applicable.

Data Availability Statement: The 3D mosaic presented in this study is openly available in <https://sketchfab.com/3d-models/caesarea-roman-underwater-harbour-da2ca77fcf6141bb8e1261fb6f1d1187>.

Acknowledgments: The authors would like to thank the IQUA Robotics team for guidance and assistance with technical issues, to Leonid Dehter for assistance with hardware integration, to Jacob Sharvit and Dror Palner from the Marine Archaeology Unit of the Israel Antiquities Authority. Special thanks also go to the support of NVIDIA Corporation through the donation of the Titan XP GPU used for 3D model generation.

Conflicts of Interest: The authors declare no conflict of interest.

References

- Pizarro, O.; Friedman, A.; Bryson, M.; Williams, S.B.; Madin, J. A simple, fast, and repeatable survey method for underwater visual 3D benthic mapping and monitoring. *Ecol. Evol.* **2017**, *7*, 1770–1782.
- Tolimieri, N.; Clarke, M.E.; Singh, H.; Goldfinger, C. Evaluating the SeaBED AUV for monitoring groundfish in untrawlable habitat. In *Marine Habitat Mapping Technology for Alaska*; Alaska Sea Grant: Fairbanks, AK, USA, 2008; pp. 129–141.
- Gracias, N.; Ridaou, P.; Garcia, R.; Escartín, J.; l'Hour, M.; Cibecchini, F.; Campos, R.; Carreras, M.; Ribas, D.; Palomeras, N.; et al. Mapping the Moon: Using a lightweight AUV to survey the site of the 17th century ship 'La Lune'. In Proceedings of the 2013 MTS/IEEE OCEANS, Bergen, Norway, 10–14 June 2013.
- Albiez, J.; Joyeux, S.; Gaudig, C.; Hilljegerdes, J.; Kroffke, S.; Schoo, C.; Arnold, S.; Mimoso, G.; Alcantara, P.; Saback, R.; et al. Flatfish—a compact subsea-resident inspection AUV. In Proceedings of the OCEANS 2015 MTS/IEEE, Washington, DC, USA, 19–22 October 2015.
- Vidal, E.; Palomeras, N.; Carreras, M. Online 3D underwater exploration and coverage. In Proceedings of the 2018 IEEE/OES Autonomous Underwater Vehicle Workshop (AUV), Porto, Portugal, 6–9 November 2018.
- Ludvigsen, M.; Sortland, B.; Johnsen, G.; Singh, H. Applications of geo-referenced underwater photo mosaics in marine biology and archaeology. *Oceanogr* **2007**, *20*, 140–149.
- Pizarro, O.; Singh, H. Toward large-area mosaicing for underwater scientific applications. *IEEE J. Ocean. Eng.* **2003**, *28*, 651–672.
- Prados, R.; Garcia, R.; Gracias, N.; Escartin, J.; Neumann, L. A novel blending technique for underwater gigamosaicing. *IEEE J. Ocean. Eng.* **2012**, *37*, 626–644.
- Pyo, J.; Cho, H.; Joe, H.; Ura, T.; Yu, S.C. Development of hovering type AUV “Cyclops” and its performance evaluation using image mosaicing. *Ocean Eng.* **2015**, *109*, 517–530.
- Houts, S.E.; Rock, S.M.; McEwen, R. Aggressive terrain following for motion-constrained AUVs. In Proceedings of the IEEE/OES Autonomous Underwater Vehicles AUV, Southampton, UK, 24–27 September 2012.
- Song, Y.; Nakath, D.; She, M.; Köser, K. Optical Imaging and Image Restoration Techniques for Deep Ocean Mapping: A Comprehensive Survey. *PFG–J. Photogramm. Remote Sens. Geoinf. Sci.* **2022**, 1–25. <https://doi.org/10.1007/s41064-022-00206-y>.
- Pinto, A.M.; Matos, A.C. MARESyE: A hybrid imaging system for underwater robotic applications. *Inf. Fusion* **2020**, *55*, 16–29.
- Kwasnitschka; et al. DeepSurveyCam—A deep ocean optical mapping system. *Sensors* **2016**, *16*, 164.
- Viswanathan, V.K.; Lobo, Z.; Lupanow, J.; von Fock, S.S.; Wood, Z.; Gambin, T.; Clark, C. AUV motion-planning for photogrammetric reconstruction of marine archaeological sites. In Proceedings of the 2017 IEEE International Conference on Robotics and Automation (ICRA), Singapore, 29 May–3 June 2017; IEEE: Piscataway, NJ, USA, 2017; pp. 5096–5103.
- Preston, V.; Salumäe, T.; Kruusmaa, M. Underwater confined space mapping by resource-constrained autonomous vehicle. *J. Field Robot.* **2018**, *35*, 1122–1148.
- Noguchi, Y.; Sakamaki, T.; Ito, S.; Humblet, M.; Furushima, Y.; Maki, T. Wide area seafloor imaging by a low-cost AUV. In Proceedings of the Global Oceans 2020: Singapore–US Gulf Coast, Biloxi, MS, USA, 5–30 October 2020; IEEE: Piscataway, NJ, USA, 2020; pp. 1–7.
- Iscar, E.; Barbalata, C.; Goumas, N.; Johnson-Roberson, M. Towards low cost, deep water AUV optical mapping. In Proceedings of the OCEANS 2018 MTS/IEEE Charleston, Charleston, SC, USA, 22–25 October 2018; IEEE: Piscataway, NJ, USA, 2018; pp. 1–6.
- Wu, J.; Bingham, R.C.; Ting, S.; Yager, K.; Wood, Z.J.; Gambin, T.; Clark, C.M. Multi-AUV motion planning for archeological site mapping and photogrammetric reconstruction. *J. Field Robot.* **2019**, *36*, 1250–1269.
- Okamoto, A.; Seta, T.; Sasano, M.; Inoue, S.; Ura, T. Visual and Autonomous Survey of Hydrothermal Vents Using a Hovering-Type AUV: Launching Hobalin Into the Western Offshore of Kumejima Island. *Geochem. Geophys. Geosyst.* **2019**, *20*, 6234–6243.
- Modasshir, M.; Rahman, S.; Youngquist, O.; Rekleitis, I. Coral identification and counting with an autonomous underwater vehicle. In Proceedings of the 2018 IEEE International Conference on Robotics and Biomimetics (ROBIO), Kuala Lumpur, Malaysia, 12–15 December 2018; IEEE: Piscataway, NJ, USA, 2018; pp. 524–529.
- Turner, J.A.; Babcock, R.C.; Hovey, R.; Kendrick, G.A. AUV-based classification of benthic communities of the Ningaloo shelf and mesophotic areas. *Coral Reefs* **2018**, *37*, 763–778.

22. Ribas, D.; Palomeras, N.; Ridao, P.; Carreras, M.; Mallios, A. Girona 500 AUV: From survey to intervention. *IEEE/ASME Trans. Mechatron.* **2011**, *17*, 46–53.
23. Williams, S.B.; Pizarro, O.; How, M.; Mercer, D.; Powell, G.; Marshall, J.; Hanlon, R. Surveying nocturnal cuttlefish camouflage behaviour using an AUV. In Proceedings of the 2009 IEEE International Conference on Robotics and Automation, Kobe, Japan, 12–17 May 2009; IEEE: Piscataway, NJ, USA, 2009; pp. 214–219.
24. Cruz, N.A.; Matos, A.C.; Almeida, R.M.; Ferreira, B.M.; Abreu, N. TriMARES—a hybrid AUV/ROV for dam inspection. In Proceedings of the OCEANS’11 MTS/IEEE KONA, Waikoloa, HI, USA, 19–22 September 2011; IEEE: Piscataway, NJ, USA, 2011; pp. 1–7.
25. Singh, W.; Örnólfsson, E.B.; Stefansson, G. A small-scale comparison of Iceland scallop size distributions obtained from a camera based autonomous underwater vehicle and dredge survey. *PLoS ONE* **2014**, *9*, e109369.
26. Jaffre, F.; Littlefield, R.; Grund, M.; Purcell, M. Development of a new version of the remus 6000 autonomous underwater vehicle. In Proceedings of the OCEANS 2019-Marseille, Marseille, France, 17–20 June 2019; IEEE: Piscataway, NJ, USA, 2019; pp. 1–7.
27. Bakken, E.M.; Midtgaard, Ø. Underwater Image Mosaics for AUV-Mounted Cameras. In Proceedings of the Global Oceans: Singapore–US Gulf Coast, Biloxi, MS, USA, 5–30 October 2020; IEEE: Piscataway, NJ, USA, 2020; pp. 1–6.
28. Madureira, L.; Sousa, A.; Braga, J.; Calado, P.; Dias, P.; Martins, R.; Pinto, J.; Sousa, J. The light autonomous underwater vehicle: Evolutions and networking. In Proceedings of the 2013 MTS/IEEE OCEANS-Bergen, Bergen, Norway, 10–14 June 2013; IEEE: Piscataway, NJ, USA, 2013; pp. 1–6.
29. Packard, G.E.; Stokey, R.; Christenson, R.; Jaffre, F.; Purcell, M.; Littlefield, R. Hull inspection and confined area search capabilities of REMUS autonomous underwater vehicle. In Proceedings of the OCEANS 2010 MTS/IEEE, Seattle, WA, USA, 20–23 September 2010.
30. Carreras, M.; Hernández, J.D.; Vidal, E.; Palomeras, N.; Ribas, D.; Ridao, P. SPARUS II AUV—A hovering vehicle for seabed inspection. *IEEE J. Ocean. Eng.* **2018**, *43*, 344–355.
31. Quigley, M.; Conley, K.; Gerkey, B.; Faust, J.; Foote, T.; Leibs, J.; Wheeler, R.; Ng, A.Y. Ros: An open-source robot operating system. *ICRA Workshop Open Source Softw.*, **2009**, *3*, 5.
32. Xia, Y.; Xu, K.; Li, Y.; Xu, G.; Xiang, X. Improved line-of-sight trajectory tracking control of under-actuated AUV subjects to ocean currents and input saturation. *Ocean Eng.* **2019**, *174*, 14–30.
33. Treibitz, T.; Schechner, Y.; Kunz, C.; Singh, H. Flat refractive geometry. *IEEE Trans. Pattern Anal. Mach. Intell.* **2011**, *34*, 51–65.
34. Fossen, T.I. *Handbook of Marine Craft Hydrodynamics and Motion Control*; Wiley: Hoboken, NJ, USA, 2011.
35. Carlton, J. *Marine Propellers and Propulsion*; Butterworth-Heinemann: Oxford, UK, 2018.
36. Van Manen, J.D. Recent research on propellers in nozzles. *Int. Shipbuild. Prog.* **1957**, *4*, 395–424.
37. Palmer, A.R. Analysis of the Propulsion and Manoeuvring Characteristics of Survey-Style AUVs and the Development of a Multi-Purpose AUV. Ph.D. Thesis, University of Southampton, Southampton, UK, 2009.
38. Horner, S. *Fluid Dynamic Drag, Practical Information on Aerodynamic Drag and Hydrodynamic Resistance*; Hoerner Fluid Dynamics: Midland Park, NJ, USA, 1965.
39. Hoerner, S.F.; Borst, H.V. Fluid-dynamic lift: practical information on aerodynamic and hydrodynamic lift. *STIA* **1975**, *76*, 32167.
40. Cardenas, P.; de Barros, E.A. Estimation of AUV hydrodynamic coefficients using analytical and system identification approaches. *IEEE J. Ocean. Eng.* **2019**, *45*, 1157–1176.
41. Prestero, T.T.J. Verification of a Six-Degree of Freedom Simulation Model for the REMUS Autonomous Underwater Vehicle. Ph.D. Thesis, Massachusetts Institute of Technology, Cambridge, MA, USA, 2001.
42. de Kruif, B.J.; Ypma, E. Self-Propulsion Parameter Identification for Control of Marin’s AUV. In Proceedings of the IEEE/OES Autonomous Underwater Vehicles Symposium (AUV), St. Johns, NL, Canada, 30 September–2 October 2020; pp. 1–6.
43. Allotta, B.; Costanzi, R.; Pugi, L.; Ridolfi, A. Identification of the main hydrodynamic parameters of Typhoon AUV from a reduced experimental dataset. *Ocean Eng.* **2018**, *147*, 77–88.
44. Johansen, T.A.; Fossen, T.I. Control allocation—A survey. *Automatica* **2013**, *49*, 1087–1103.
45. Khan, H.Z.I.; Rajput, J.; Ahmed, S.; Sarmad, M.; Sharjil, M. Robust control of overactuated autonomous underwater vehicle. In Proceedings of the 2018 15th International Bhurban Conference on Applied Sciences and Technology (IBCAST), Islamabad, Pakistan, 9–13 January 2018; pp. 269–275.
46. Palomeras, N.; Vallicrosa, G.; Mallios, A.; Bosch, J.; Vidal, E.; Hurtos, N.; Carreras, M.; Ridao, P. AUV homing and docking for remote operations. *Ocean Eng.* **2018**, *154*, 106–120.